*Astronomy & Astrophysics* manuscript no. main
January 13, 2026
©ESO 2026

# Cosmoglobe DR2. VII. Towards a concordance model of large-scale thermal dust emission for microwave and infrared frequencies

E. Gjerløw[1]⋆, R. M. Sullivan[1], R. Aurvik[1], A. Basyrov[1], L. A. Bianchi[1], A. Bonato[2], M. Brilenkov[1], H. K. Eriksen[1], U. Fuskeland[1], M. Galloway[1], K. A. Glasscock[1], L. T. Hergt[3], D. Herman[1], J. G. S. Lunde[1], A. I. Silva Martins[1], M. San[1], D. Sponseller[4], N.-O. Stutzer[1], H. Thommesen[1], V. Vikenes[1], D. J. Watts[1], I. K. Wehus[1], and L. Zapelli[2,5,6]

[1] Institute of Theoretical Astrophysics, University of Oslo, Blindern, Oslo, Norway
[2] Dipartimento di Fisica, Università degli Studi di Milano, Via Celoria, 16, Milano, Italy
[3] Laboratoire de Physique des 2 infinis – Irène Joliot Curie (IJCLab), Orsay, France
[4] Department of Space, Earth and Environment, Chalmers University of Technology, Gothenburg, Sweden
[5] Università di Trento, Università degli Studi di Milano, CUP E66E23000110001
[6] INFN sezione di Milano, 20133 Milano, Italy

January 13, 2026

arXiv:2601.07822v1 [astro-ph.CO] 12 Jan 2026

**ABSTRACT**

We fit a four-component thermal dust model to *COBE*-DIRBE data between 3.5 and 240 $\mu$m within the global Bayesian end-to-end Cosmoglobe DR2 reanalysis. Following a companion analysis of *Planck* HFI, the four components of this model correspond to "hot dust", "cold dust", "nearby dust", and "H$\alpha$ correlated dust", respectively, and each component is modelled in terms of a fixed spatial template and a spatially isotropic spectral energy density (SED) defined by an overall free amplitude for each DIRBE channel. Except for the cold dust amplitude, which is only robustly detected in the 240 $\mu$m channel, we measure statistically significant template amplitudes for all components in all DIRBE channels between 12 and 240 $\mu$m. In the 3.5 and 4.9 $\mu$m channels, only the hot component is detected, while the 1.25 and 2.2 $\mu$m channels are too dominated by starlight emission to allow robust dust detections. The total number of DIRBE-specific degrees of freedom in this model is 25. Despite this low dimensionality, the resulting total SED agrees well with recent `astrodust` predictions. At both low and high frequencies, more than 95 % of the frequency map variance is captured by the model, while at 60 and 100 $\mu$m about 70 % of the signal variance is successfully accounted for. The hot dust component, which in a companion paper has been found to correlate strongly with C II emission, has the highest absolute amplitude in all DIRBE frequency channels; in particular, at 3.5 $\mu$m, which is known to be dominated by polycyclic aromatic hydrocarbon emission, this component accounts for at least 80 % of the total signal. This analysis represents an important step towards establishing a joint concordance model of thermal dust emission applicable to both the microwave and infrared regimes.

**Key words.** ISM: general - Zodiacal dust, Interplanetary medium - Cosmology: observations, diffuse radiation - Galaxy: general

## 1. Introduction

In a series of seven companion papers, within which this is the last, we have reanalyzed the 30-year-old *COBE*-DIRBE data using modern end-to-end Bayesian statistical techniques as implemented in the Cosmoglobe[1] framework. From this work, a set of ten full-sky DIRBE frequency maps has emerged (Watts et al. 2024a), covering the infrared frequency range between 1.25 and 240 $\mu$m. These maps have both substantially lower systematic errors and better error characterization compared to their official counterparts (Hauser et al. 1998; Watts et al. 2024a), and, in particular, they suffer far less from zodiacal light contamination (Kelsall et al. 1998; San et al. 2024). As a result they can be used for more detailed astrophysics applications. A few examples of this are presented in the current paper suite, including improved estimates of the cosmic infrared background (CIB) spectrum (Watts et al. 2024b) and large-scale starlight emission (Galloway et al. 2026).

The main topic of the last three papers in the series (Gjerløw et al. (2026); Sullivan et al. (2026); and the present paper) is global modelling of thermal dust radiation on large angular scales in the microwave and infrared frequency regimes. This issue has been the focus of intense scrutiny ever since the groundbreaking IRAS (Neugebauer et al. 1984) measurements were published in 1982, and its scientific importance has only increased through the release of a series of increasingly sensitive data sets, such as *COBE*-DIRBE (Hauser et al. 1998) and *Planck* HFI (Planck Collaboration III 2020). Today, detailed dust modelling plays a key role in many of the most competitive fields of cosmology, from the search for inflationary gravitational waves in cosmic microwave background (CMB) *B*-mode polarization data (Ade et al. 2021) to measurements of dark energy using distant supernovae (Popovic et al. 2025).

As of today, *Planck* HFI defines the state-of-the-art for full-sky thermal dust mapping, both in terms of signal-to-noise ratio as well as systematic control. Based on *Planck*'s nine frequency channels, the team produced several exquisite dust models in both intensity and polarization (Planck Collaboration Int. XVII 2014; Planck Collaboration XI 2014; Planck Collaboration Int. XIV 2014; Planck Collaboration Int. XIX 2015; Planck Collaboration X 2016; Planck Collaboration Int. XXII 2015; Planck Collaboration XI 2020; Planck Collaboration XII 2020), and these now form the basis for much of the dust modelling efforts in the

⋆ Corresponding author: E. Gjerløw; eirik.gjerlow@astro.uio.no
[1] http://cosmoglobe.uio.no

field (e.g., Thorne et al. 2017; Zonca et al. 2021). However, at the same time, the relatively narrow frequency range of *Planck*, covering only 30-857 GHz, implies that the applicability of these models is currently quite limited. Furthermore, the absolute calibration of the 857 GHz *Planck* channel, which is nominally the most sensitive *Planck* dust channel, is uncertain at the ∼10 % level (Planck Collaboration III 2020; Planck Collaboration LVII 2020), and this induces a large uncertainty on the dust spectral energy density (SED) parameters when extrapolating to higher frequencies.

In the current paper, we address these issues by fitting the multi-component dust model proposed by Gjerløw et al. (2026) and Sullivan et al. (2026) to the re-processed *COBE*-DIRBE data within the Cosmoglobe DR2 analysis framework. This model consists of four primary components, namely 1) cold dust, 2) hot dust, 3) nearby dust, and 4) H$\alpha$-correlated dust (which observed in extinction). From the previous papers, this model is already known to fit the *Planck* HFI frequencies very well when coupled to simple modified blackbody (MBB) SEDs with spatially constant spectral parameters, and in this paper we show that the same spatial morphologies also trace dust in the DIRBE frequencies with high precision, although with more complicated SED behaviour. The combined result is a global model that jointly describes both microwave and infrared frequencies.

So far, this model has only been developed for and applied to intensity measurements. However, polarized thermal dust emission also plays a key role in modern astrophysics and cosmology. For instance, massive resources are currently being spent on searching for and constraining the amplitude of inflationary gravitational waves through deep CMB *B*-mode polarization experiments (LiteBIRD Collaboration et al. 2023; Ade et al. 2019), and polarized thermal dust emission represents a key challenge for these (Fuskeland et al. 2023). Given the high efficiency of the Cosmoglobe DR2 four-component dust model for intensity data, it is reasonable to expect a similar performance for polarization observations.

## 2. Bayesian modelling of thermal dust emission in Cosmoglobe DR2

The following work is part of Cosmoglobe Data Release 2, and represents as such a global Bayesian analysis exploration of the joint posterior of all involved parameters. The following analysis is thus intricately bound together with the other papers, both in terms of the data sets and the data model used. Hence, we will in the following only give a brief recap of the underlying data model and algorithms, while paying special attention to the thermal dust model. For full details, we refer the interested reader to Watts et al. (2024a) and references therein.

### 2.1. Data model

In the parametric Bayesian Cosmoglobe framework (e.g., BeyondPlanck Collaboration 2023; Watts et al. 2023, 2024a), the first step is to write down an explicit parametric model that incorporates all known aspects of the dataset with which we are working, including both instrumental and astrophysical effects. The main target of the current analysis are the DIRBE time-ordered data (TOD), and we adopt the following model for these,

$$\begin{aligned} \boldsymbol{d}_{\mathrm{DIRBE}}(\nu) &= \mathsf{GPB} \sum_{c=1}^{n_{\mathrm{comp}}} \mathsf{M}_c(\nu)\boldsymbol{a}_c + \boldsymbol{s}_{\mathrm{zodi}}(\nu) + \boldsymbol{s}_{\mathrm{static}}(\nu) + \boldsymbol{n} \\ &\equiv \boldsymbol{s}^{\mathrm{tot}} + \boldsymbol{n}_{\mathrm{corr}} + \boldsymbol{n}_{\mathrm{w}}. \end{aligned} \tag{1}$$

Here $\nu$ is the frequency of a given data channel; $\boldsymbol{d}$ is a vector containing the full TOD; $\mathsf{G}$ is an overall gain factor; $\mathsf{P}$ is the pointing matrix which projects the pixelated sky onto a $n_{\mathrm{tod}}$-sized space; $\mathsf{B}$ is the instrumental beam convolution operator; and $\boldsymbol{n}_{\mathrm{corr}}$ and $\boldsymbol{n}_{\mathrm{w}}$ represents instrumental correlated and white noise, respectively, with spectral parameters $\xi_{\mathrm{n}}$, most importantly the white noise rms per TOD sample.

The physical sky is represented by three terms. Firstly, the sum over $c$ includes all stationary sky components, such as Galactic dust or free-free emission. Each of these are modelled in terms of a mixing matrix, $\mathsf{M}_c$, that describes the relative amplitude of the given component as a function of frequency, and an amplitude map, $\boldsymbol{a}$. Secondly, $\boldsymbol{s}_{\mathrm{zodi}}(\nu)$ describes zodiacal emission, i.e., emission from dust grains within the Solar system (Kelsall et al. 1998; San et al. 2024). Because these grains are located so close to the Earth, this component must be modelled dynamically by taking into account the observatory's position in the Solar system as a function of time. Finally $\boldsymbol{s}_{\mathrm{static}}$ accounts for emission that appears static in Solar-centric coordinates, which for instance could be due to either errors in the zodiacal light model or DIRBE sidelobes. These two last terms are discussed extensively by Watts et al. (2024a) and San et al. (2024). In the present work, however, we focus on the first of the three terms.

### 2.2. Multi-component thermal dust modelling

Interstellar dust — amorphous particles of silicate and carbonaceous materials — makes its presence known on practically all astrophysically relevant wavelengths. Understanding this material is interesting in its own right, however, it is also crucial to improve astrophysical foreground removal, especially when interstellar dust emission contaminates other signals of interest (e.g., Hensley & Draine 2021).

Recently, a major step forward in this direction was made by Hensley & Draine (2023), who introduced the so-called "astrodust+PAH" model, wherein the diffuse interstellar medium (ISM) was hypothesized to be made up of a single composite material (the eponymous astrodust) for scales larger than $\sim$ 0.02 $\mu$m, and a distinct variety of materials — including so-called polycyclic aromatic hydrocarbons (PAH) — on scales smaller than this. In the wavelength regime between 3000 – 100 $\mu$m, this model is well described by an MBB SED [2], i.e., an SED that follows

$$s(\nu) \propto \nu^{\beta} B(\nu, T), \tag{2}$$

where $\nu$ is the frequency, $B$ is the Planck law for a perfect blackbody with temperature $T$, and $\beta$ is the spectral index. Typical ISM temperatures are around ∼20 K, for which the SED typically peaks around 150 $\mu$m or ∼2000 GHz. At shorter wavelengths (2.5 $\mu$m to 12 $\mu$m), the astrodust+PAH model is dominated by nanoscale particle emission, and exhibits strong emission lines at various wavelengths (see, e.g., Fig. 10 in Hensley & Draine 2023).

#### 2.2.1. The four-component Cosmoglobe DR2 dust model

The astrodust model provides a physically well understood framework for modelling Galactic thermal dust emission. Typically, in a given line-of-sight, the relative contribution of various dust components will vary. At the same time, the degree to which such variations can be detected and described is limited

[2] The actual astrodust model is made up of a composite MBB which has a transition between 353 and 217 GHz

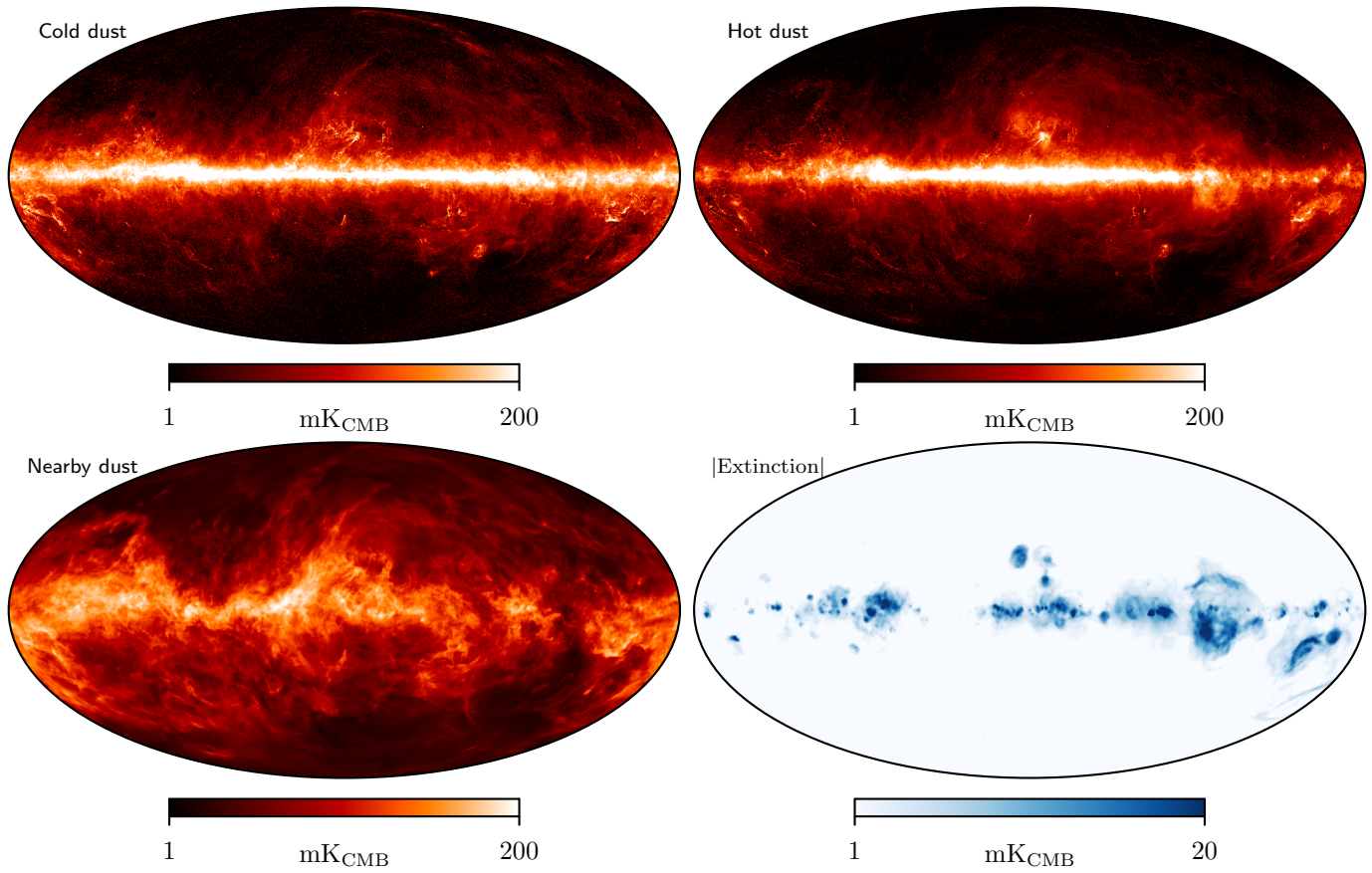


**Fig. 1.** Dust template maps used in the Cosmoglobe DR2 sky model, whose units are defined with the *Planck* HFI 545-1 bolometer channel as the reference frequency. From left to right and top to bottom, the four panels show 1) the cold dust template, $\boldsymbol{t}_{\rm cold}$; 2) the hot dust template, $\boldsymbol{t}_{\rm hot}$; 3) the nearby dust template, $\boldsymbol{t}_{\rm nearby}$; and 4) the (absolute value of the) $\rm H_\alpha$-correlated dust extinction template, $\boldsymbol{a}_{\rm H\alpha}$. All panels employ the *Planck* non-linear high dynamic range color scheme, defined by $\log_{10}((\boldsymbol{t} + \sqrt{4 + \boldsymbol{t}^2})/2)$, which results in a nearly linear behaviour for small values and exponential for large values.

by the resolution and signal-to-noise ratios of the available data at the wavelengths involved. Thus, classifying populations of interstellar dust with common spectral parameters has been of high importance.

It was demonstrated by Gjerløw et al. (2026) that a natural and highly effective classification of such populations can be achieved through the use of templates derived from surveys of spectral line emission (C II, H$\alpha$, CO and H I) and from inference of nearby dust structures via starlight extincion (Edenhofer et al. 2024). In that paper, we showed that a linear combination of five such templates could explain more than 95% of the large-scale dust signal variance in the *Planck* 353–857 GHz and DIRBE 240–60 $\mu$m channels; at 25–12 $\mu$m it accounted for more than 80% of the signal variance.

A notable short-coming of the analysis of Gjerløw et al. (2026) was its low angular resolution, determined by the 7° FWHM FIRAS beam. Aiming to improve on this issue, Sullivan et al. (2026) therefore derived high-resolution maps of the cold (HI-correlated) and hot (CII-correlated) components through a high-dimensional posterior grid search. Together with the *Gaia* extinction template Edenhofer et al. (2024) and the H$\alpha$ template (Haffner et al. 2003), which are natively provided with a resolution appropriate for DIRBE analysis, the resulting set of four templates provides a useful basis set for modelling dust throughout the DIRBE frequency range. These templates are plotted in Fig. 1.

While analyzing the HFI data with this model, Sullivan et al. (2026) found that the SED of all four components could be very well approximated by MBB spectra throughout the HFI frequency range. However, when extending into the higher-frequency DIRBE range, non-thermal physics becomes increasingly important, and a simple parametric SED is no longer valid. Instead, for the DIRBE frequency range we define a set of SED bins, each of which is roughly chosen to correspond to the width of a DIRBE band, as shown in Table 1. Each dust component is then defined to have a constant amplitude within a given bin, resulting in one free parameter per bin per component.

**Table 1.** Components enabled for each frequency band. The dust band widths represent the width of each dust band used in this analysis, not the instrumental bandwidths.

| Band | Bin width (GHz) | Hot | Cold | Nearby | H$\alpha$ |
|---|---|---|---|---|---|
| DIRBE 240 $\mu$m | 617 | ✓ | ✓ | ✓ | ✓ |
| DIRBE 140 $\mu$m | 873 | ✓ | | ✓ | ✓ |
| DIRBE 100 $\mu$m | 1524 | ✓ | | ✓ | ✓ |
| DIRBE 60 $\mu$m | 4936 | ✓ | | ✓ | ✓ |
| DIRBE 25 $\mu$m | 9100 | ✓ | | ✓ | ✓ |
| DIRBE 12 $\mu$m | 27400 | ✓ | | ✓ | ✓ |
| DIRBE 4.9 $\mu$m | 24715 | ✓ | | ✓ | |
| DIRBE 3.5 $\mu$m | 39275 | ✓ | | ✓ | |

Based on this model, the Cosmoglobe DR2 sky model (i.e., the third term of Eq. (1)) takes the following form,

$$\begin{aligned}
\sum_{c=1}^{n_{\rm comp}} \mathsf{M}_c(\nu)\boldsymbol{a}_c =& [a]_{\rm cold}(\nu)\boldsymbol{t}_{\rm cold} && \text{(Cold dust)}\\
&+[a]_{\rm hot}(\nu)\boldsymbol{t}_{\rm hot} && \text{(Hot dust)}\\
&+[a]_{\rm nearby}(\nu)\boldsymbol{t}_{\rm nearby} && \text{(Nearby dust)}\\
&+[a]_{\rm H\alpha}(\nu)\boldsymbol{t}_{\rm H\alpha} && \text{(H}\alpha\text{ correlated dust)}\\
&+\left(\frac{\nu_{0,\rm ff}}{\nu}\right)^2 \frac{g_{\rm ff}(\nu;T_{\rm e})}{g_{\rm ff}(\nu_{0,\rm ff};T_{\rm e})}\boldsymbol{t}_{\rm ff} && \text{(Free-free)}\\
&+U_{\rm mJy}\sum_{j=1}^{n_{\rm s}} f_{Gaia,j}a_{{\rm s},j} && \text{(Bright stars)}\\
&+U_{\rm mJy}f_{Gaia,j}\boldsymbol{a}_{{\rm fs},j} && \text{(Faint stars)}\\
&+m_\nu && \text{(Monopole).}
\end{aligned} \tag{3}$$

In this equation, the bracketed amplitudes, $[a](\nu)$, indicate the binned SED amplitudes discussed above, while $\boldsymbol{t}_i$ represents the corresponding template maps as shown in Fig. 1. The first four terms in this equation form our model of thermal dust, which is the main focus of this work. The fifth term models the free-free emission, which contributes only a small contribution at all relevant frequencies. The sixth and seventh terms represent two point source contributions (primarily stars), which are described in detail by Galloway et al. (2026). Finally, the last term represents the zero-level at each frequency, which ideally should represent the CIB monopole (Watts et al. 2024b).

### 2.3. Bayesian end-to-end analysis

Taking into account both the general data model in Eq. 1 and the sky model in Eq. 3, the full set of free parameters in the Cosmoglobe DR2 analysis is $\omega = \{\mathsf{G}, \zeta_{\rm zodi}, \boldsymbol{s}_{\rm static}, [a]_{\rm cold}, [a]_{\rm hot}, [a]_{\rm nearby}, [a]_{\rm H\alpha}, a_{s,i}, \xi_{\rm c}, m_\nu\}$, and the goal is now to estimate these jointly by drawing samples from the posterior distribution (Watts et al. 2024a) — that is, we aim to map out $P(\omega|\boldsymbol{d})$, the probability distribution of the set of parameters $\theta$ given the observed data $\boldsymbol{d}$. Bayes' theorem allows us to write this on the following form,

$$P(\omega|\boldsymbol{d}) = \frac{P(\boldsymbol{d}|\omega)P(\omega)}{P(\boldsymbol{d})}. \tag{4}$$

In this equation, $P(\boldsymbol{d}|\omega)$ is called the likelihood; $P(\omega)$ is called the prior; and $P(\boldsymbol{d})$ is called the evidence. While the latter plays an important role in Bayesian model selection applications, we are in the current work only concerned with parameter optimization, and the evidence is then just a normalization constant.

The number of parameters involved in $\omega$ is large, and the correlations between the various components are complicated, and this makes sampling from the posterior function a highly non-trivial task. The Cosmoglobe framework is based on the `Commander` software (Eriksen et al. 2004; Seljebotn et al. 2019; Galloway et al. 2023), which maps out the posterior parameter distribution through a process called Gibbs sampling (e.g., Geman & Geman 1984), a Monte-Carlo method based on sequentially sampling each parameter (or a subset of parameters) from their respective marginal distributions with respect to all other parameters. The theory of Gibbs sampling then guarantees that by iterating over all conditional distributions, the resulting multivariate sample sets will represent a proper sample from the true joint distribution. For the Cosmoglobe DR2 analysis, the Gibbs chain looks as follows:

$$\begin{aligned}
\mathsf{G} &\leftarrow P(\mathsf{G} &&|\boldsymbol{d}, && \xi_n, [a]_i, && \boldsymbol{a}_{{\rm s},i}, \zeta_{\rm z}, && \boldsymbol{a}_{\rm static})\\
\xi_{\rm n} &\leftarrow P(\xi_{\rm n} &&|\boldsymbol{d}, && \mathsf{G}, [a]_i, && \boldsymbol{a}_{{\rm s},i}, \zeta_{\rm z}, && \boldsymbol{a}_{\rm static})\\
[a]_i &\leftarrow P([a]_i &&|\boldsymbol{d}, && \mathsf{G}, \xi_n, && \boldsymbol{a}_{{\rm s},i}, \zeta_{\rm z}, && \boldsymbol{a}_{\rm static})\\
\boldsymbol{a}_{{\rm s},i} &\leftarrow P(\boldsymbol{a}_{{\rm s},i} &&|\boldsymbol{d}, && \mathsf{G}, \xi_n, [a]_i, && \zeta_{\rm z}, && \boldsymbol{a}_{\rm static})\\
\zeta_{\rm z} &\leftarrow P(\zeta_{\rm z} &&|\boldsymbol{d}, && \mathsf{G}, \xi_n, [a]_i, && \boldsymbol{a}_{{\rm s},i}, && \boldsymbol{a}_{\rm static})\\
\boldsymbol{a}_{\rm static} &\leftarrow P(\boldsymbol{a}_{\rm static} &&|\boldsymbol{d}, && \mathsf{G}, \xi_n, [a]_i, && \boldsymbol{a}_{{\rm s},i}, \zeta_{\rm z} && )
\end{aligned} \tag{5}$$

Here, the symbol $\leftarrow$ indicates the operation of drawing a sample from the distribution on the right-hand side (see Watts et al. (2024a) for a complete overview of all the symbols in this equation) . After some burn-in period, the resulting joint parameter sets will correspond to samples drawn from the true underlying joint posterior.

Since every step of the Gibbs sampling process assumes that all other parameters are "given", we can now treat the fully interconnected problem (i.e., sampling from the joint posterior of all parameters involved in our data model) as a modular one – meaning that we can perform each "sub-analysis" without being concerned with the other parts of the problem. Hence, in this paper, we mainly focus on the four first components of Eq. (3), leaving the treatment of stars to Galloway et al. (2026); monopoles to Watts et al. (2024b); zodiacal light to San et al. (2024); and condition on free-free emission as determined by Planck Collaboration X (2016).

As far as the current paper is concerned, the critical step is therefore to be able sample from $P([a]_i|\boldsymbol{d},\ldots)$. The actual likelihood for this distribution is given by first subtracting all other physical components from the raw data, and then noting that the residual should ideally be given by white noise. The appropriate likelihood is therefore the following Gaussian,

$$\mathcal{L}([a]_i) \equiv P(\boldsymbol{d}|[a]_i,\ldots) \propto e^{-\frac{1}{2}\sum_\nu\left(\frac{\boldsymbol{r}_\nu - [a]_i t_i}{\sigma_\nu}\right)^2}, \tag{6}$$

where $\boldsymbol{r}_\nu$ denotes the data-minus-signal residual obtained by subtracting all other model components except the currently sampled one, and $\sigma_\nu$ is the instrumental noise rms per TOD sample. We impose no prior on the amplitudes, and therefore the conditional distribution is identical to this likelihood.

To sample from this distribution, we implement a standard Metropolis MCMC accept-reject sampler. That is, at each step we propose an updated value of $[a]_i$, with a small pre-defined step size; evaluate Eq. 6; and accept the new point with probability $a = \min(\mathcal{L}_{\rm new}/\mathcal{L}_{\rm old}, 1)$. To obtain reasonable accept rates, we typically choose a large step size in preliminary exploratory

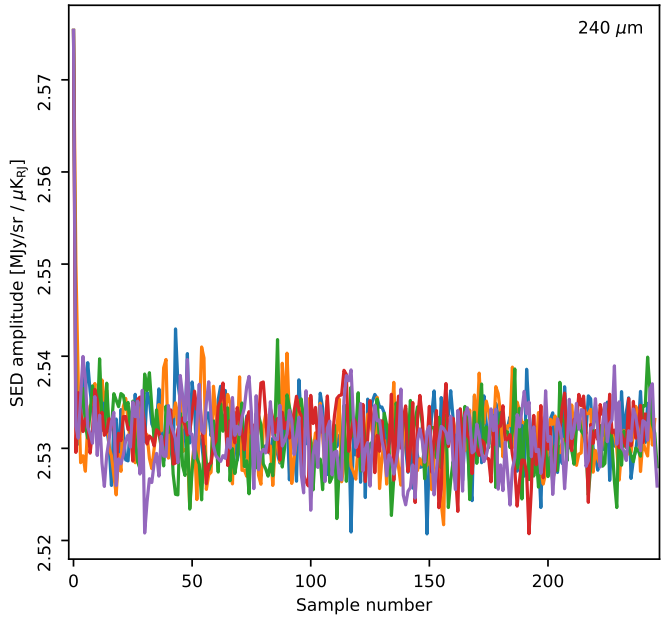


**Fig. 2.** Cold dust amplitude as a function of iteration for the 240 $\mu$m channel where it is included. The five lines correspond to the five independent sampling chains in the analysis. We see robust mixing in all chains.

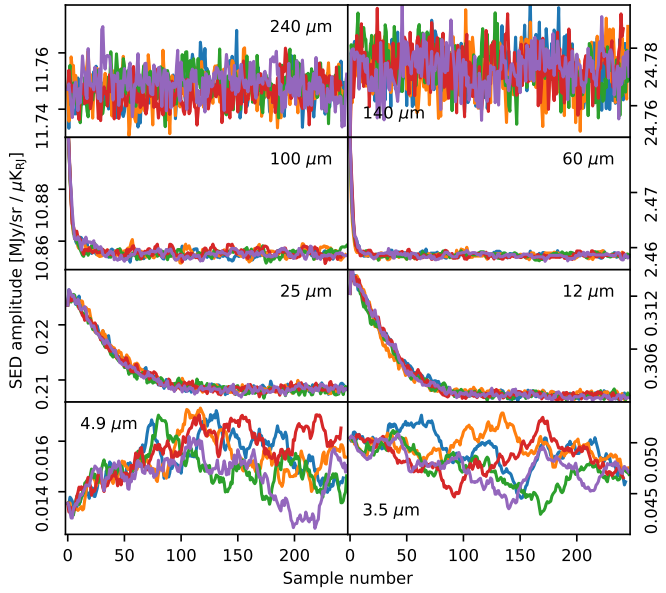


**Fig. 3.** Hot dust amplitudes as a function of iteration for the eight lowest frequency DIRBE channels, with all five sampling chains overplotted. We see that the 3.5 $\mu$m and 4.9 $\mu$m channels exhibit slower mixing than the others, but still manage to explore the full parameter space.

runs; terminate the analysis when no further improvements are made; and restart from the previous best-fit solution with a smaller Metropolis step size.

## 3. Data

There are three main datasets used directly in the Cosmoglobe DR2 analysis, namely low-level data from *COBE*-DIRBE, starlight positions from WISE (Wright et al. 2010), and starlight parameters from *Gaia* (Gaia Collaboration et al. 2016, 2018).

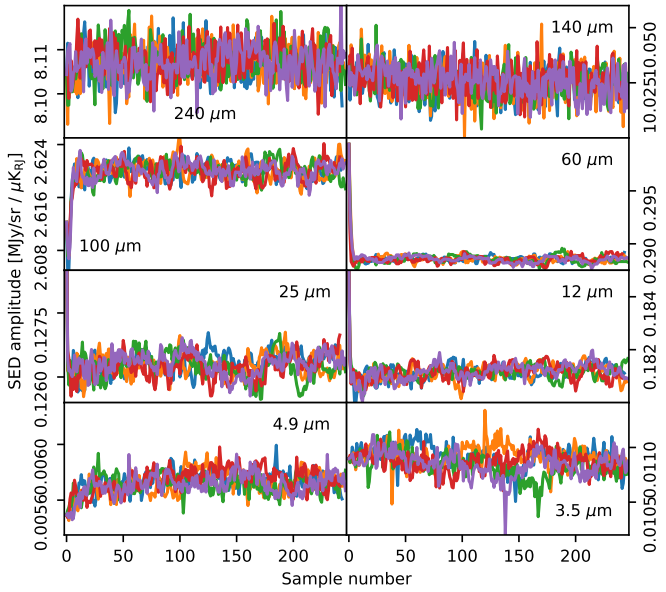


**Fig. 4.** Nearby dust amplitudes as a function of the iteration for the six lowest frequency DIRBE channels, with all five sampling chains overplotted. We see robust mixing in all chains and for all frequency channels.

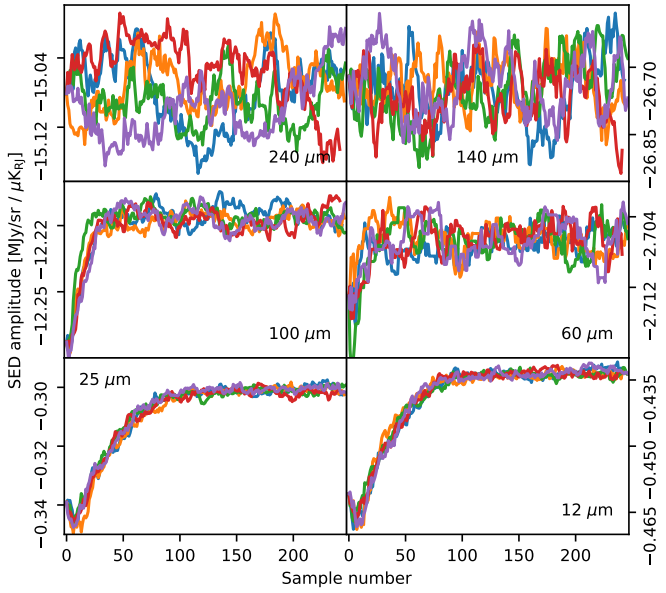


**Fig. 5.** H$\alpha$ dust amplitudes as a function of the iteration for the six lowest frequency DIRBE channels, with all five sampling chains overplotted. The 240 and 140 $\mu$m channels exhibit slower mixing than the others, but still manage to explore the full parameter space.

These are supplemented by our own dust templates, which are drawn from the analysis performed in Sullivan et al. (2026), and incorporate data from *Planck* HFI and *Gaia*. Below we give a succinct description of these data sets and the preprocessing performed; for a more in-depth description, see Watts et al. (2024a) and Galloway et al. (2026).

### 3.1. COBE-DIRBE

The Diffuse InfraRed Explorer (DIRBE), whose main goal was the mapping out of the cosmic infrared background, was part of

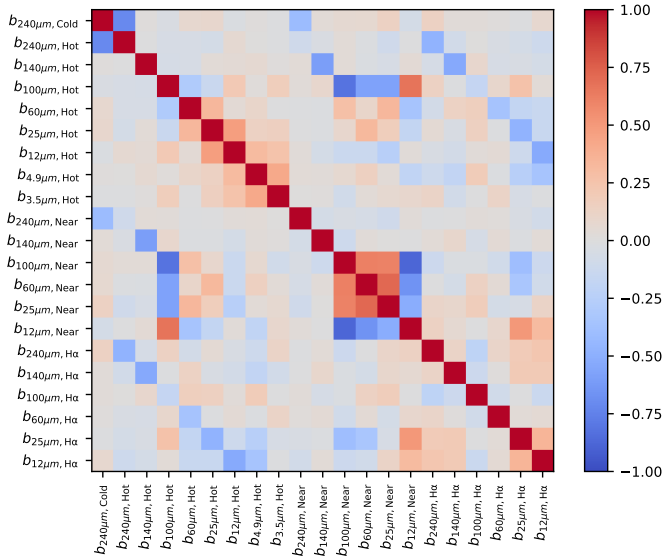


**Fig. 6.** Correlations between the dust amplitudes at each frequency, as computed over the full sample set. They are largely uncorrelated, but there are some structures within some bands as the sampler trades off between components (e.g., 240 $\mu$m in the upper left). There is also some fainter structure in the nearby dust amplitudes across channels.

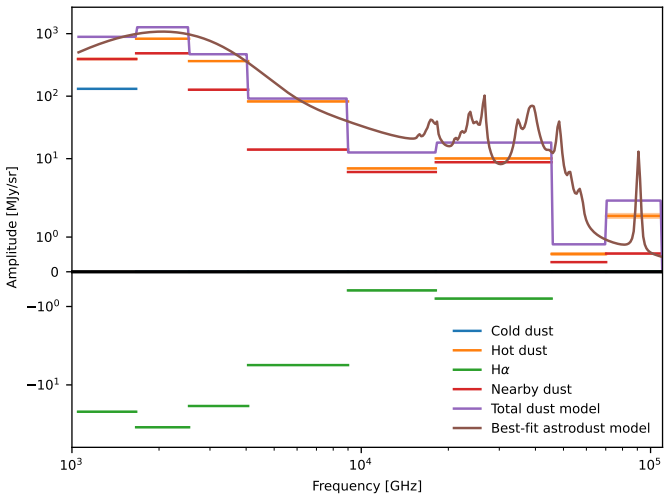


**Fig. 7.** The total dust SED as a function of frequency, as well as the four dust components. The best-fit astrodust model fit to the total SED for the frequencies shown is also plotted in brown.

the *COBE* satellite (Boggess et al. 1992; Silverberg et al. 1993), and measured the sky in ten frequency bands from 1.25 $\mu$m to 240 $\mu$m. In this analysis, we have converted the original DIRBE CIO (Calibrated Individual Observations), whose pointing information is given in terms of Quadcube pixels with a resolution of 20′′ into HEALPix $N_{\mathrm{side}}$=512 pixelation maps, resulting in an approximate angular resolution of 42′. Following the nomenclature of Watts et al. (2024a), we refer to the DIRBE CIOs as "time-ordered data" (TOD). Performing our analysis on DIRBE TOD directly allows us to target the zodiacal light (San et al. 2024), which, as mentioned above, must be treated as a time-dependent sky component, in contrast to other astrophysical sources.

**Table 2.** Summary of dust template amplitude posterior constraints.

| Component (Thermal dust band) | Template amplitude [MJy/sr] |
|---|---|
| Cold dust (240 $\mu$m) | 131.03 ± 0.16 |
| H$\alpha$-correlated dust (240 $\mu$m) | −26.853 ± 0.065 |
| H$\alpha$-correlated dust (140 $\mu$m) | −47.613 ± 0.119 |
| H$\alpha$-correlated dust (100 $\mu$m) | −21.754 ± 0.007 |
| H$\alpha$-correlated dust (60 $\mu$m) | −4.819 ± 0.003 |
| H$\alpha$-correlated dust (25 $\mu$m) | −0.536 ± 0.002 |
| H$\alpha$-correlated dust (12 $\mu$m) | −0.772 ± 0.001 |
| Nearby dust (240 $\mu$m) | 392.383 ± 0.182 |
| Nearby dust (140 $\mu$m) | 485.184 ± 0.336 |
| Nearby dust (100 $\mu$m) | 126.808 ± 0.062 |
| Nearby dust (60 $\mu$m) | 13.964 ± 0.015 |
| Nearby dust (25 $\mu$m) | 6.113 ± 0.014 |
| Nearby dust (12 $\mu$m) | 8.770 ± 0.020 |
| Nearby dust (4.9 $\mu$m) | 0.278 ± 0.003 |
| Nearby dust (3.5 $\mu$m) | 0.526 ± 0.005 |
| Hot dust (240 $\mu$m) | 393.585 ± 0.180 |
| Hot dust (140 $\mu$m) | 829.926 ± 0.242 |
| Hot dust (100 $\mu$m) | 363.674 ± 0.045 |
| Hot dust (60 $\mu$m) | 82.369 ± 0.012 |
| Hot dust (25 $\mu$m) | 6.981 ± 0.017 |
| Hot dust (12 $\mu$m) | 10.078 ± 0.009 |
| Hot dust (4.9 $\mu$m) | 0.513 ± 0.033 |
| Hot dust (3.5 $\mu$m) | 1.609 ± 0.063 |

### 3.2. WISE and Gaia

At the higher DIRBE frequency bands (25–1.25 $\mu$m), starlight emission becomes a significant source of emission, both as point sources and as a diffuse component. Using the AllWise point source catalog (Eisenhardt et al. 2020), we crossmatched the brighest stars in the $W1$ band against *Gaia* DR2, and used the estimated physical parameters from that catalogue to model the bright stars. In addition, we created a general faint source template, similar to that used in Hauser et al. (1998), based on the stars that were not part of the bright star component (see Galloway et al. (2026) for more details). Together, these two components comprise the sixth and seventh component in Eq. (3).

### 3.3. Data selection

As noted in Gjerløw et al. (2026), not all thermal dust components are expected to contribute to the DIRBE bands we are considering in this paper (i.e., 240–12$\mu$m). Following the same logic as in that paper, we restrict the dust components to be active in the various DIRBE bands as indicated in Table 1. In particular, the cold dust component peaks at 1 THz, and falls off quickly at higher frequencies, making it quicly subdominant to all other components. In contrast, the hot dust component is visible until the 3.5 $\mu$m channel, and must be included to obtain a satisfactory fit. The strength of the nearby component is intermediate, while the impact of the H$\alpha$-correlated components is restricted to a relatively small fraction of the sky.

### 3.4. Masks

As discussed by Watts et al. (2024a), analysis masks are generated based on dust residual amplitudes and zodiacal dust residuals. For the dust components, regions that are poorly modeled are excluded depending on frequency and residual amplitude. This is determined using a combination of smoothed residual maps and $\chi^2$ maps per frequency channel. This ensures that only data that are poorly modeled are masked, while retaining well-modeled

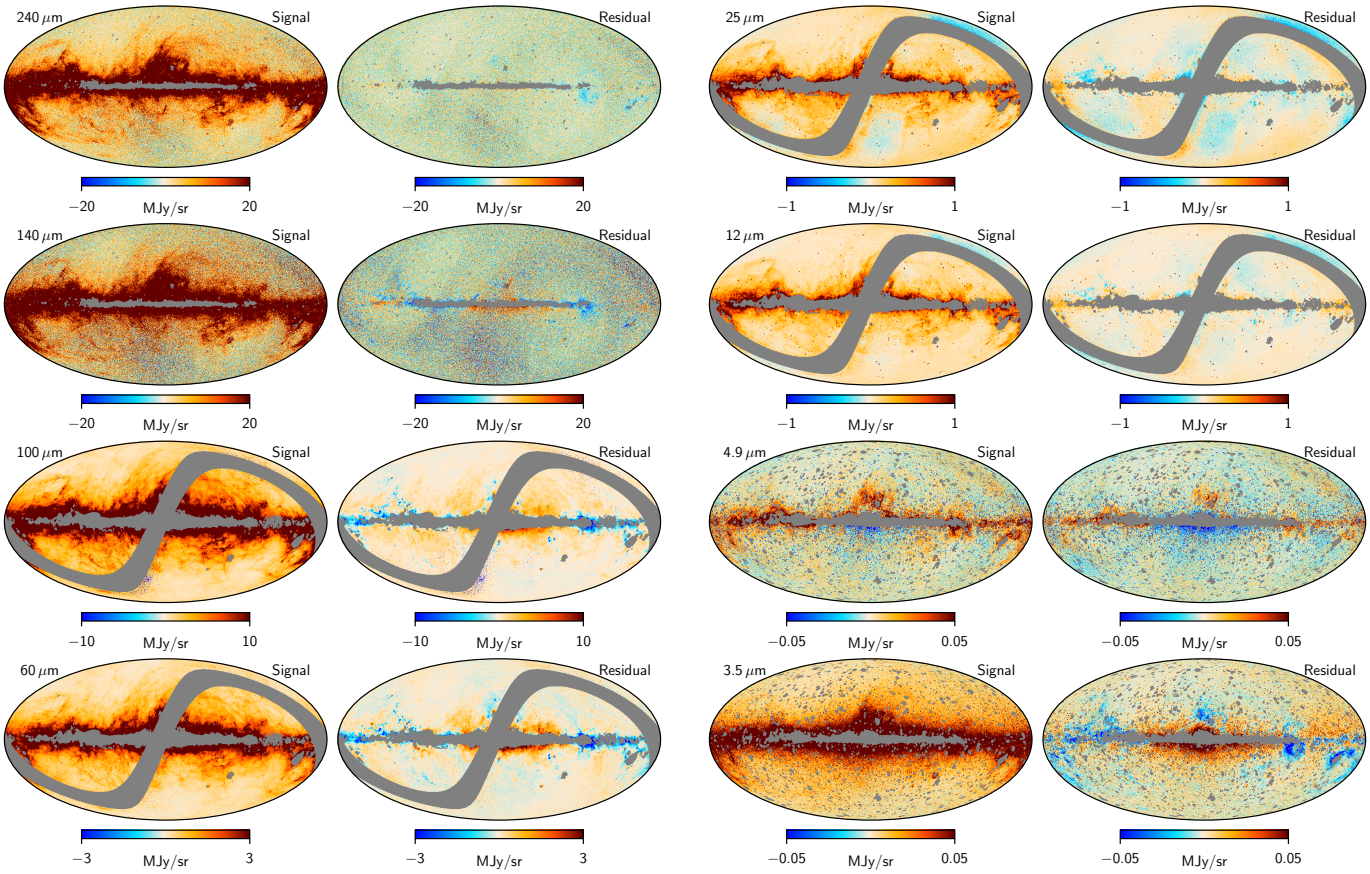


**Fig. 8.** Comparison between thermal dust frequency maps (i.e., stationary sky signal minus starlight and free-free; *first and third columns*) and residual maps for each frequency channel (*second and fourth column*). Gray pixels indicate the analysis masks used for each frequency channel.

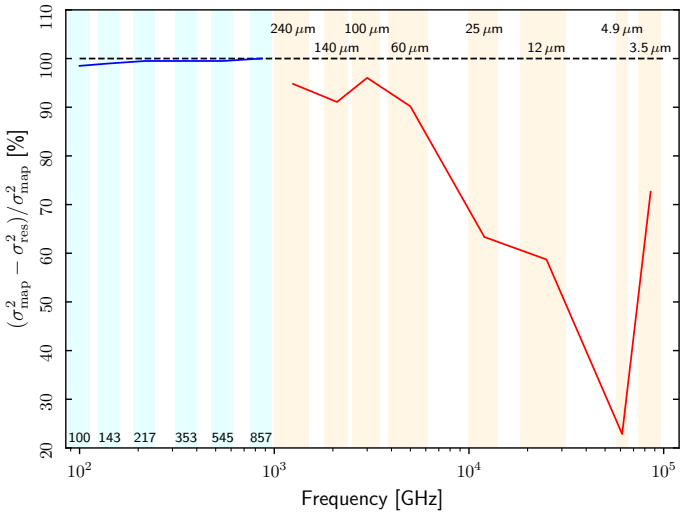


**Fig. 9.** Dust model efficiency as a function of frequency, as defined in terms of variance reduction. The red line shows results for DIRBE, as evaluated from the maps shown in Fig. 8, while the blue line shows results for *Planck* HFI, as presented by Sullivan et al. (2026). Vertical bands indicate the position and bandwidth of each DIRBE (orange) and HFI (cyan) frequency channel.

high signal-to-noise pixels. For the bands where zodiacal dust is brightest (12–100 $\mu$m), we apply an additional mask along the Ecliptic plane. This mask was determined solely by the brightest zodiacal dust channel, 25 $\mu$m, and is largely due to asteroidal band uncertainty.

## 4. Results

The Cosmoglobe DR2 production analysis resulted in five Gibbs chains, each of which contains approximately 250 samples. Out of these, the first 100 samples are considered part of the burn-in period, after which all chains have converged. In the following, we include trace plots with the burnin period included to visualize the convergence properties of the chains.

### 4.1. Markov chains, correlations and convergence

In Figs. 2 to 5, we plot the Gibbs chain traceplots for all the five Gibbs chains used in the analysis, for all four dust components. After a period of reaching equilibrium — which varies from almost instantly (for the cold dust amplitude, for example) to around 100 samples at the most (particularly evident for the hot dust and H$\alpha$-correlated dust 25 and 12 $\mu$m bins) — the chains generally do not exhibit any long correlations and seem to mix fairly well. The only exceptions are the 240 and 140 $\mu$m H$\alpha$-correlated dust bins, where we see more long-term trends that indicate a slower traversal through parameter space.

In Fig. 6, we show the correlations between the various SED bins in the run, calculated over all five chains after discarding burn-in. The strongest correlations are internally between the nearby dust bins. Most of the bins are correlated with each other, but they are anticorrelated with the 12 $\mu$m amplitude. The correlation of the nearby dust component's amplitude between different bins is due to indirect interactions of the parameters in the model, as the morphology of the nearby dust is fixed, and the amplitudes are sampled separately.

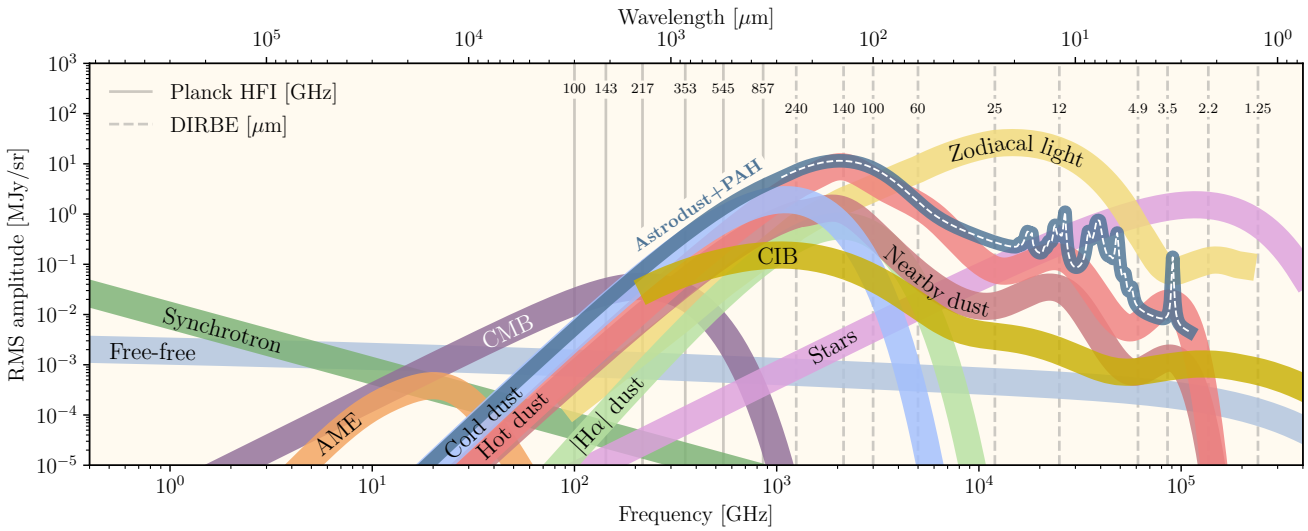


**Fig. 10.** Overview of the large-scale microwave and infrared sky from 1 GHz to 1$\mu$m, based on the Cosmoglobe DR1 and DR2 data. The four component dust model is shown, as well as the best fit astrodust model. The *Planck* HFI and DIRBE central frequencies are indicated with vertical lines.

Those same bins, and in particular the 100 $\mu$m bin, are also anticorrelated with the 100 $\mu$m hot dust amplitude. This is not unexpected, as there is morphological overlap between the hot dust and nearby dust components, as displayed in Fig. 1. Therefore, a negative correlation would be expected to model the same total amplitude in the DIRBE map itself. The same phenomenon can be seen between hot and cold dust at 240 $\mu$m.

### 4.2. Multi-component thermal dust SED posteriors

In Table 2, we summarize the thermal dust SED posteriors resulting from the above analysis as the mean value and variance of the chain samples (including all five chains of the analysis, discarding burn-in). Similarly, we plot the posterior mean values per bin in Fig. 7, where the thickness of the line indicates the standard deviation of that amplitude. In the same plot, we also show the posterior total SED, wherein all four components are summed up, as well as the Astrodust+PAH model that is the best fit to the mean total dust SED.[3]

Both the hot dust and nearby dust components follow a typical thermal dust modified blackbody curve up to about 3000 GHz, mirroring the results found in Gjerløw et al. (2026). At higher frequencies, they exhibit the characteristic rise in the SED, where models like Astrodust+PAH predicts emission lines from the nanoscale particles. This figure also shows that fitting the total (i.e., the sum of all the components) dust model to the Astrodust+PAH model yields a curve that fits very well with the posterior mean SED values.

We cannot draw any such conclusions about the the cold dust component, as it is only active for the lowest frequency SED bin. However, the fact that the amplitude of the cold dust component is about an order of magnitude smaller than for the hot and nearby dust components at 1 THz is consistent with the results of Gjerløw et al. (2026). Future work, in conjunction with higher sensitivity datasets, such as *IRAS* and AKARI, will be useful in further determing the SED of this component.

[3] Specifically, we fit an overall amplitude $A$, as well as the $\log_{10} U$ parameter used in Hensley & Draine (2023), with the total model to fit being $A \cdot \mathrm{EM}(\log_{10} U)$, where $EM$ is their tabulated function returning the emission as a function of $\log_{10} U$.

The H$\alpha$ component, as in the previous analyses, exhibits a negative SED, and is thus representative of dust extinction rather than emission. However, it exhibits the same type blackbody spectrum with a hint of a rise towards the PAH emission region. Again, this is consistent with the results presented by Gjerløw et al. (2026).

### 4.3. Model efficiency and residuals

In Fig. 8, we show the dust frequency maps — that is, the frequency maps with starlight and free-free signal subtracted — as well as the residual maps after subtracting the four-component dust model used in this analysis. The grey pixels indicate the masks used at each frequency, as described in Sect. 3.4. In all bands, we see a weak pattern of over-and-undersubtractions in the Galactic plane, suggesting that there is room for further sophistication of the template model. For example, the Galactic plane is precisely where we would expect true spatial variations within a single dust component, which we have not allowed for in this work. To quantify this, we estimate the reduction of the RMS of the residuals with respect to the original map in Fig. 9.

For the 240–60 $\mu$m channels we find that $\gtrsim 90\,\%$ of the variance is explained by our four-component model. The first two channels are the cleanest, simply because these are closest in frequency to the *Planck* HFI data from which the cold and hot dust templates are derived, and non-thermal effects have not yet set in. Between 140 and 60 $\mu$m, the model is clearly struggling to account for emission from the Galactic center, with similar excesses and oversubtractions, characteristic of temperature variations.

For the 25 and 12 $\mu$m channels only $\sim$60 % of the signal variance is explaineed by the dust model. This can partially be explained by incomplete zodiacal dust subtraction, as evidenced by negative regions in both the signal and residual maps. Much of the residual structure is uncorrelated with the Galactic plane, indicating that dust modeling is not the primary cause of the excess residuals.

At 4.9 $\mu$m, we are limited by the variation of the starlight SEDs, detailed knowledge of the starlight SEDs, incomplete extinction corrections, and the resolution of DIRBE (Galloway

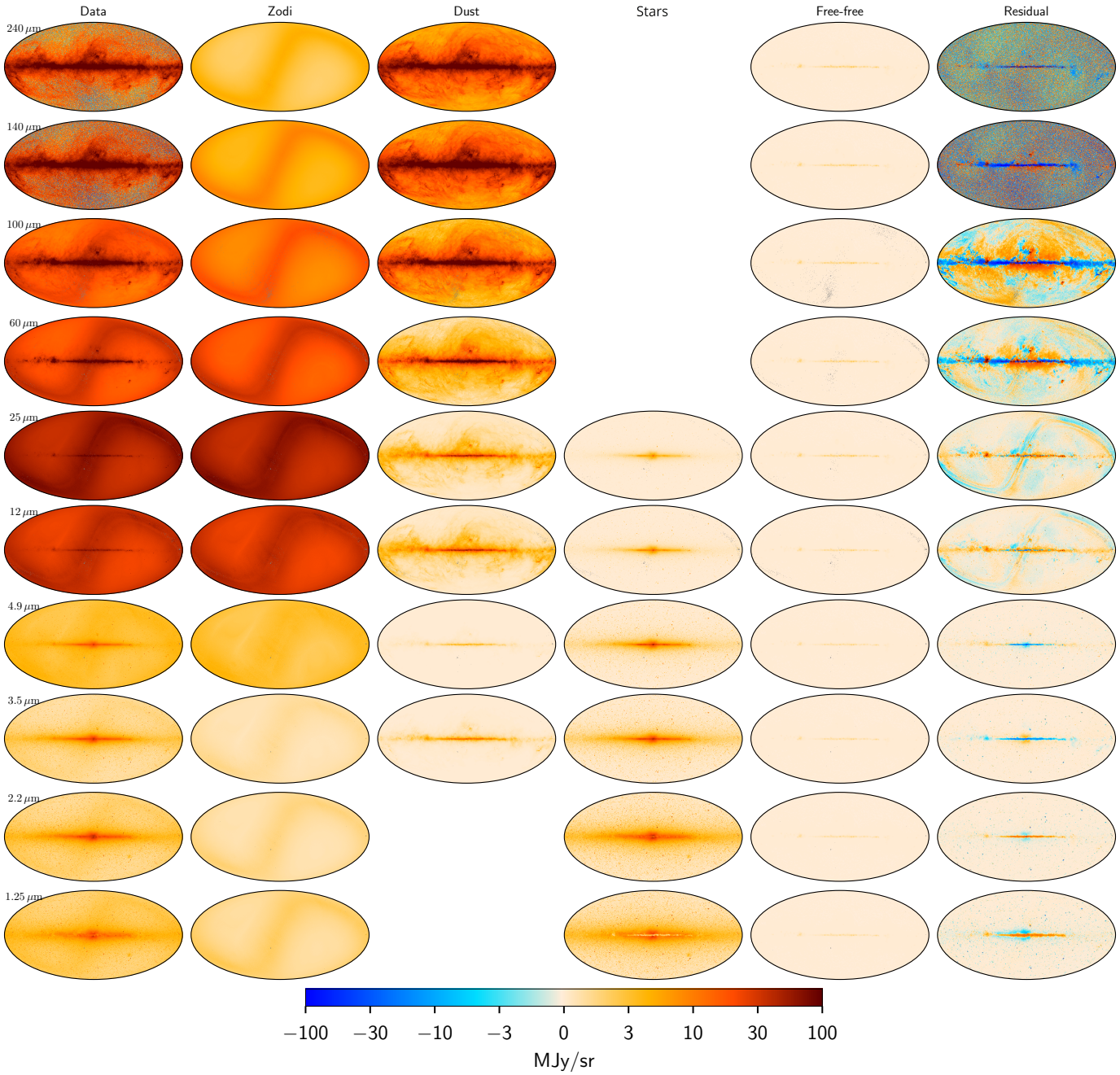


**Fig. 11.** Comparison between the re-analyzed DIRBE data and the various fitted components for one single Gibbs sample. Columns show, from left to right, 1) the time-ordered DIRBE data co-added into pixelized maps; 2) zodiacal light emission; 3) thermal dust emission; 4) star emission; 5) free-free emission; and 6) data-minus-model residual emission. Rows show individual frequency channels. Missing entries corresponds to components that are forced to zero in the model. Note that all panels are plotted with the same color scale in units of MJy/sr, and can be directly compared.

et al. 2026). Because this work is focused on thermal dust, we leave these residuals for future work. In particular, the SPHEREx (Doré et al. 2014) satellite will be able to resolve and directly measure the SED of most of the infreared-bright point sources close to the Galactic plane.

Finally, at 3.5 $\mu$m we see that more than 70 % of the signal variance is captured by the model. This is despite the fact that starlight is even stronger at 3.5 than at 4.9 $\mu$m. The explanation is simply the presence of a bright PAH line at 3.3 $\mu$m. The structure of this may be seen by eye by comparing the 3.5 and 4.9 $\mu$m signal maps in Fig. 8; while the 4.9 $\mu$m map is clearly contamined by over-subtracted starlight emission, the 3.5 $\mu$m map exhibits a bright Galactic signal with a physically reasonable morphology. That extra power is due to PAH emission, and from the residuals we see that this is also very well modelled by the hot dust template. This observations strongly suggests that correlating recent SPHEREx full-sky observations of the 3.3 $\mu$m line with *Planck* HFI and DIRBE far-infrared maps will be fruitful.

## 5. Cosmoglobe DR2 sky model

Until now, we have focused on the infrared regime of sky modeling, largely decoupled from the microwave region where Cosmoglobe was primarily developed. In this section, we unite

the *Planck* HFI-based microwave and DIRBE-based infrared regimes to present an integrated sky model that will serve as a foundation of future global dust modelling work.

In Fig. 10 we show the best-fit Cosmoglobe sky model, derived from the first and second data releases, including the four-component dust model presented in this paper. Although the amplitudes chosen are relatively arbitrary (every line of sight in the sky will potentially have different scalings), the spectral shape of the lines are directly taken from the Gibbs chains as presented in Watts et al. (2023) and Watts et al. (2024a). This plot represents the current state of the Cosmoglobe effort to create a common sky model derived with the same data pipeline.

Finally, in Fig. 11, we show the amplitude maps of all the components involved in the Cosmoglobe DR2 analysis, including zodiacal light, dust, starlight, and free-free emission. These maps represent the Cosmoglobe sky model as applied to the DIRBE bands, and in the final column we see the residual maps at each band. At the two lowest bands, where the thermal dust is the dominant sky component (see Fig. 10), the model is performing quite well (with the same caveats as for the pure dust residual maps), especially given that we essentially treat the thermal dust as a model with ∼20 free parameters, instead of fitting two spectral parameters per pixel on the sky.

## 6. Conclusions

In this paper, which is part of the second Cosmoglobe data release, we have fitted a four-component dust model to the eight lowest DIRBE frequency bands. Recent analyses (Gjerløw et al. 2026; Sullivan et al. 2026) demonstrated the feasibility and efficiency of decomposing thermal dust into a relatively low number of distinct populations with global spectral parameters.

The model uses a nearby dust template and H$\alpha$ dust template presented in Gjerløw et al. (2026), labeled "nearby dust", and "H$\alpha$-correlated dust", as well as two template components derived in Sullivan et al. (2026), labeled "Hot dust", "Cold dust" respectively. The SED of each component was defined as a constant bin over each DIRBE band. We found that the resulting total SED is a good match to the Astrodust+PAH model, and that the nanoparticle emission at high frequencies is detected in these components. As in previous analyses, the H$\alpha$-correlated component absorbs rather than emits radiation, and thus has a negative SED.

Finally, we present the current state of the Cosmoglobe sky model, ranging from a few GHz to $\sim 10^3$ THz, and containing diverse components, such as the CMB, synchrotron radiation, zodiacal light, starlight, the various thermal dust components, and the CIB. Although the current results are already very encouraging, this work represents only a first step towards a global dust model for the radio, microwave, and infrared regimes. Perhaps the most immediate improvements will come from incorporating complementary high-resolution and -sensitivity infrared experiments, for instance AKARI (Murakami et al. 2007). This will allow the construction of dust templates that can also be used for analysis of high-resolution CMB experiments such as Simons Observatory (Ade et al. 2019).

Likewise, integrating WISE and SPHEREx data will be a game-changer in our ability to separate starlight from Galactic emission between 1 and 10 $\mu$m, as well as unique identification of individual PAH lines. Given the strong association we have found between the 3.5 $\mu$m channel and the hot dust component already in this paper, joint analysis between *Planck* and SPHEREx stands out as a potential goldmine for broad-spectrum dust modelling. and dust

These results also raise intruiging questions regarding dust modelling for CMB *B*-mode experiments that search for the imprint of primordial gravitational waves. The fact that a simple four-component dust model works this will for intensity measurements strongly suggests that a similar approach could work for polarization. In that case, it is worth considering the prospects of establishing corresponding polarization templates as the four employed here. First, cold dust dominates below 1000 GHz, and most high-precision CMB experiments will therefore naturally measure this component within their default frequency range. In order to map hot dust, however, it is important to have access to higher frequencies, and as shown by (Sullivan et al. 2026) using HFI data, a maximum frequency of 857 GHz works very well. Assessing how much the separation between hot and cold dust degrades if one only had access to at most, say, 353 or 545 GHz data would be very interesting. Moving on to the nearby dust component, full-sky polarized starlight measurements is key. Such data are already in the process of being generated by the PASIPHAE experiment (Tassis et al. 2018), and these could easily become a cornerstone in the analysis of all future *B*-mode experiments. Finally, the most challenging template to establish in polarization would be the H$\alpha$ tracer, simply because H$\alpha$ is expected to be extremely weakly polarized. At the same time, this does not automatically imply that impact of the H$\alpha$ template would be negligible in polarization, simply because it appears in absorption, and the physical mechanism that causes that effect is just as likely to absorbe any photon, regardless of their polarization direction. On the other hand, it is also important to note that the H$\alpha$ template has a limited effective footprint on the sky, and are mostly associated with structures at low Galactic latitudes. The affected regions may therefore most likely be efficiently masked in a future high-precision *B*-mode analysis.

Overall, we conclude that the current analysis opens up new and exciting research avenues for global dust modelling from radio to infrared frequencies. Many of these are already under active exploration, and will be reported through future Cosmoglobe data releases.

*Acknowledgements.* We thank Richard Arendt, Tony Banday, Johannes Eskilt, Dale Fixsen, Ken Ganga, Paul Goldsmith, Shuji Matsuura, Sven Wedemeyer, Janet Weiland and Edward Wright for useful suggestions and guidance. The current work has received funding from the European Union's Horizon 2020 research and innovation programme under grant agreement numbers 819478 (ERC; Cosmoglobe), 772253 (ERC; bits2cosmology), 101165647 (ERC, Origins), 101141621 (ERC, Commander), and 101007633 (MSCA; CMBInflate). This article reflects the views of the authors only. The funding body is not responsible for any use that may be made of the information contained therein. This research is also funded by the Research Council of Norway under grant agreement numbers 344934 (YRT; CosmoglobeHD) and 351037 (FRIPRO; LiteBIRD-Norway). Some of the results in this paper have been derived using healpy (Zonca et al. 2019) and the HEALPix (Górski et al. 2005) packages. We acknowledge the use of the Legacy Archive for Microwave Background Data Analysis (LAMBDA), part of the High Energy Astrophysics Science Archive Center (HEASARC). HEASARC/LAMBDA is a service of the Astrophysics Science Division at the NASA Goddard Space Flight Center. This publication makes use of data products from the Wide-field Infrared Survey Explorer, which is a joint project of the University of California, Los Angeles, and the Jet Propulsion Laboratory/California Institute of Technology, funded by the National Aeronautics and Space Administration. This work has made use of data from the European Space Agency (ESA) mission *Gaia* (https://www.cosmos.esa.int/gaia), processed by the *Gaia* Data Processing and Analysis Consortium (DPAC, https://www.cosmos.esa.int/web/gaia/dpac/consortium). Funding for the DPAC has been provided by national institutions, in particular the institutions participating in the *Gaia* Multilateral Agreement. We acknowledge the use of data provided by the Centre d'Analyse de Données Etendues (CADE), a service of IRAP-UPS/CNRS (http://cade.irap.omp.eu, Paradis et al. 2012). This paper and related research have been conducted during and with the support of the Italian national inter-university PhD programme in Space Science and Technology. Work on this article was produced while attend-

ing the PhD program in PhD in Space Science and Technology at the University of Trento, Cycle XXXIX, with the support of a scholarship financed by the Ministerial Decree no. 118 of 2nd March 2023, based on the NRRP - funded by the European Union - NextGenerationEU - Mission 4 "Education and Research", Component 1 "Enhancement of the offer of educational services: from nurseries to universities" - Investment 4.1 "Extension of the number of research doctorates and innovative doctorates for public administration and cultural heritage" - CUP E66E23000110001.

## References

Ade, P., Aguirre, J., Ahmed, Z., et al. 2019, J. Cosmology Astropart. Phys., 2019, 056
Ade, P. A. R., Ahmed, Z., Amiri, M., et al. 2021, Phys. Rev. Lett., 127, 151301
BeyondPlanck Collaboration. 2023, A&A, 675, A1
Boggess, N. W., Mather, J. C., Weiss, R., et al. 1992, ApJ, 397, 420
Doré, O., Bock, J., Ashby, M., et al. 2014, arXiv e-prints, arXiv:1412.4872
Edenhofer, G., Zucker, C., Frank, P., et al. 2024, A&A, 685, A82
Eisenhardt, P. R. M., Marocco, F., Fowler, J. W., et al. 2020, ApJS, 247, 69
Eriksen, H. K., O'Dwyer, I. J., Jewell, J. B., et al. 2004, ApJS, 155, 227
Fuskeland et al. 2023, A&A, in preparation [arXiv:20xx.xxxxx]
Gaia Collaboration et al. 2016, A&A, 595, A1
Gaia Collaboration et al. 2018, A&A, 616, A1
Galloway, M., Andersen, K. J., Aurlien, R., et al. 2023, A&A, 675, A3
Galloway, M. et al. 2026, A&A, in preparation [arXiv:20xx.xxxxx]
Geman, S. & Geman, D. 1984, IEEE Trans. Pattern Anal. Mach. Intell., 6, 721
Gjerløw et al. 2026, A&A, in preparation [arXiv:20xx.xxxxx]
Górski, K. M., Hivon, E., Banday, A. J., et al. 2005, ApJ, 622, 759
Haffner, L. M., Reynolds, R. J., Tufte, S. L., et al. 2003, ApJS, 149, 405
Hauser, M. G., Arendt, R. G., Kelsall, T., et al. 1998, ApJ, 508, 25
Hensley, B. S. & Draine, B. T. 2021, ApJ, 906, 73
Hensley, B. S. & Draine, B. T. 2023, ApJ, 948, 55
Kelsall, T., Weiland, J. L., Franz, B. A., et al. 1998, ApJ, 508, 44
LiteBIRD Collaboration, Allys, E., Arnold, K., et al. 2023, Progress of Theoretical and Experimental Physics, 2023, 042F01
Murakami, H., Baba, H., Barthel, P., et al. 2007, PASJ, 59, S369
Neugebauer, G., Habing, H. J., van Duinen, R., et al. 1984, ApJ, 278, L1
Paradis, D., Dobashi, K., Shimoikura, T., et al. 2012, A&A, 543, A103
Planck Collaboration XI. 2014, A&A, 571, A11
Planck Collaboration X. 2016, A&A, 594, A10
Planck Collaboration III. 2020, A&A, 641, A3
Planck Collaboration XI. 2020, A&A, 641, A11
Planck Collaboration XII. 2020, A&A, 641, A12
Planck Collaboration Int. XIV. 2014, A&A, 564, A45
Planck Collaboration Int. XVII. 2014, A&A, 566, A55
Planck Collaboration Int. XIX. 2015, A&A, 576, A104
Planck Collaboration Int. XXII. 2015, A&A, 576, A107
Planck Collaboration LVII. 2020, A&A, 643, A42
Popovic, B., Shah, P., Kenworthy, W. D., et al. 2025, arXiv e-prints, arXiv:2511.07517
San, M. et al. 2024, A&A, in preparation [arXiv:20xx.xxxxx]
Seljebotn, D. S., Bærland, T., Eriksen, H. K., Mardal, K. A., & Wehus, I. K. 2019, A&A, 627, A98
Silverberg, R. F., Hauser, M. G., Boggess, N. W., et al. 1993, in Society of Photo-Optical Instrumentation Engineers (SPIE) Conference Series, Vol. 2019, Infrared Spaceborne Remote Sensing, ed. M. S. Scholl, 180–189
Sullivan et al. 2026, A&A, in preparation [arXiv:20xx.xxxxx]
Tassis, K., Ramaprakash, A. N., Readhead, A. C. S., et al. 2018, arXiv e-prints, arXiv:1810.05652
Thorne, B., Dunkley, J., Alonso, D., & Næss, S. 2017, MNRAS, 469, 2821
Watts, D., Galloway, M., Gjerlow, E., et al. 2024a, A&A, submitted [arXiv:2408.10952]
Watts, D. et al. 2024b, A&A, in preparation [arXiv:2406.01491]
Watts, D. J., Basyrov, A., Eskilt, J. R., et al. 2023, A&A, 679, A143
Wright, E. L., Eisenhardt, P. R. M., Mainzer, A. K., et al. 2010, AJ, 140, 1868
Zonca, A., Singer, L., Lenz, D., et al. 2019, Journal of Open Source Software, 4, 1298
Zonca, A., Thorne, B., Krachmalnicoff, N., & Borrill, J. 2021, Journal of Open Source Software, 6, 3783